Asymmetric Hurricane Boundary Layer Structure from Dropsonde Composites in Relation to the Environmental Vertical Wind Shear

JUN A. ZHANG

NOAA/AOML/Hurricane Research Division, and Rosenstiel School of Marine and Atmospheric Science, University of Miami, Miami, Florida

ROBERT F. ROGERS, PAUL D. REASOR, ERIC W. UHLHORN, AND FRANK D. MARKS JR.

NOAA/AOML/Hurricane Research Division, Miami, Florida

(Manuscript received 19 November 2012, in final form 6 May 2013)

ABSTRACT

This study investigates the asymmetric structure of the hurricane boundary layer in relation to the environmental vertical wind shear in the inner core region. Data from 1878 GPS dropsondes deployed by research aircraft in 19 hurricanes are analyzed in a composite framework. Kinematic structure analyses based on Doppler radar data from 75 flights are compared with the dropsonde composites. Shear-relative quadrant-mean composite analyses show that both the kinematic and thermodynamic boundary layer height scales tend to decrease with decreasing radius, consistent with previous axisymmetric analyses. There is still a clear separation between the kinematic and thermodynamic boundary layer heights. Both the thermodynamic mixed layer and height of maximum tangential wind speed are within the inflow layer. The inflow layer depth is found to be deeper in quadrants downshear, with the downshear right (DR) quadrant being the deepest. The mixed layer depth and height of maximum tangential wind speed are alike at the eyewall, but are deeper outside in quadrants left of the shear. The results also suggest that air parcels acquire equivalent potential temperature θ_e from surface fluxes as they rotate through the upshear right (UR) quadrant from the upshear left (UL) quadrant. Convection is triggered in the DR quadrant in the presence of asymmetric mesoscale lifting coincident with a maximum in θ_e. Energy is then released by latent heating in the downshear left (DL) quadrant. Convective downdrafts bring down cool and dry air to the surface and lower θ_e again in the DL and UL quadrants. This cycling process may be directly tied to shear-induced asymmetry of convection in hurricanes.

1. Introduction

Vertical shear of the environmental wind is one of the most important factors influencing tropical cyclone (TC) development and maintenance at all phases of the TC life cycle. As a result, effects of the environmental wind shear on TC intensity and structure have been extensively studied both in numerical simulations and observations. For example, tropical cyclone intensity is found to be correlated with environmental vertical wind shear (e.g., Kaplan and DeMaria 2003; Kaplan et al. 2010).

Mechanisms for shear-induced intensity change include warm core ventilation (Simpson and Riehl 1958; Tang and Emanuel 2010, 2012), development of convective asymmetry (Frank and Ritchie 2001; Ritchie and Frank 2007), balanced-dynamical response of the vortex to vertical tilting (DeMaria 1996; Jones 1995, 2000; Reasor and Montgomery 2001; Reasor et al. 2004), and asymmetric organization of eyewall mesovortices and convective cells (e.g., Schubert et al. 1999; Braun et al. 2006; Braun and Wu 2007; Reasor et al. 2009). In sheared TCs, the azimuthal location of the convection is usually related to the direction of the shear, exhibiting a pronounced convective asymmetry with maximum convection located in the downshear left quadrant of the eyewall. Such a relationship between the direction of environmental wind shear and eyewall convection is a common feature both of observed (e.g., Reasor et al. 2000; Heymsfield et al. 2001; Black et al. 2002; Corbosiero and Molinari 2003; Eastin et al. 2005; Molinari and Vollaro 2010; Reasor and Eastin 2012) and simulated (e.g., Wang and Holland 1996;

Corresponding author address: Dr. Jun Zhang, NOAA/AOML/Hurricane Research Division, University of Miami/CIMAS, 4301 Rickenbacker Causeway, Miami, FL 33149.
E-mail: jun.zhang@noaa.gov

DOI: 10.1175/MWR-D-12-00335.1

Bender 1997; Frank and Ritchie 2001; Rogers et al. 2003; Braun and Wu 2007; Davis et al. 2008) TCs.

Recently, Riemer et al. (2010) proposed an intensity modification mechanism by vertical wind shear, relating the convective asymmetry outside the eyewall to the asymmetric balanced dynamics governing a vertically sheared vortex. They argued that the balanced vorticity asymmetry associated with vortex tilting organizes convection through frictional convergence. In their simulations, the convective downdrafts in the outer core region transport low equivalent potential temperature θ_e air into the inflow layer, which in turn affects hurricane intensification. Shelton and Molinari (2009) found that abnormally dry air upshear generated a large radial gradient of θ_e ($6\,\mathrm{K\,km^{-1}}$) just outside the eyewall of Hurricane Claudette (2003) and hypothesized that cold downdrafts associated with the mixing of this dry air into the core caused the weakening of the hurricane. This argument is consistent with the downward flux of low-entropy air in the simulation of sheared storms given by Riemer et al. (2010). However, this argument is different from that given by Cione et al. (2013), who found that drier near-surface conditions (leading to lower θ_e) were associated with intensifying storms using extensive in situ buoy data in hurricanes.

Despite the abovementioned studies on shear and TCs, the effects of shear on the atmospheric boundary layer are still not well known. In particular, how the boundary layer thermodynamic structure varies in response to the environmental shear is poorly understood. Until now, although many observational studies have documented boundary layer structure in a sheared system (e.g., Powell 1990; Cione et al. 2000; Kepert 2006a,b; Bell and Montgomery 2008; Sitkowski and Barnes 2009; Molinari et al. 2013), how the boundary layer structure varies as a function of azimuth with respect to the shear direction is not well documented. As the boundary layer plays an important role in the energy transport processes of a hurricane (e.g., Ooyama 1969; Emanuel 1986, 1995; Rotunno et al. 2009; Bryan and Rotunno 2009; Smith et al. 2009; Smith and Montgomery 2010; Bryan 2012), it is essential to understand the relationship between the environmental wind shear and the boundary layer processes.

As an extension of our previous study on the axisymmetric structure of the hurricane boundary layer with emphasis on the characteristic height scales (Zhang et al. 2011), this study is the first attempt to investigate the possible relationship between environmental wind shear and hurricane boundary layer structure in the inner core region using observational data. We analyze over 1800 global positioning system (GPS) dropsonde data collected by National Oceanic and Atmospheric Administration (NOAA) research aircraft in 19 hurricanes. Doppler radar data analysis reported by Reasor et al. (2013) provides independent confirmation of the kinematic structure and rainfall asymmetry in response to the wind shear. As part of NOAA's Hurricane Forecast Improvement Project (HFIP), this work also expands previously analyzed datasets for the purpose of evaluating boundary layer structure representation in model simulations.

The objectives of this paper are as follows:

1) to document the inner core boundary layer asymmetric structure relative to the environmental vertical wind shear in a composite framework;
2) to investigate the asymmetry of the characteristic boundary layer height scales in four quadrants relative to the shear direction; and
3) to investigate the possible connection between the shear-induced asymmetry of convection and low-level thermodynamic structure.

2. Data and analysis method

The dropsonde data used in this study were collected by a total of 208 NOAA research flights in 19 hurricanes, which extends the dataset as used by Zhang et al. (2011) and Zhang and Uhlhorn (2012). Details of the dropsonde instrumentation can be found in Hock and Franklin (1999). The dropsonde measures air temperature, relative humidity, pressure, and horizontal and vertical wind speed. Typical observation errors for pressure, temperature, and relative humidity are 1.0 hPa, 0.2°C, and 5%, respectively. The fall speed of a sonde is 12–14 $\mathrm{m\,s^{-1}}$, while the typical sampling rate is 2 Hz. For consistency, the dropsonde data have been postprocessed and quality-controlled using the National Center for Atmospheric Research's (NCAR's) Atmospheric Sounding Processing Environment (ASPEN) software. Recent studies have indicated that little difference exists between the Editsonde- and ASPEN-processed wind data (e.g., Barnes 2008). Although there have been several minor improvements to the dropsonde design and processing since the original documentation (Hock and Franklin 1999), overall data accuracy has not changed significantly to impact results in this study.

A total of 1878 dropsondes are utilized in the final analysis, as summarized in Table 1. These dropsondes have continuous measurements of wind speed, temperature, and humidity from the flight level to the surface (10 m) and were collected in open ocean conditions. The intensity range of each storm included in Table 1 indicates that all of the storms were of at least category 1 intensity on the Saffir–Simpson (SS) scale at the time of the

TABLE 1. Storm information and numbers of flights and dropsondes.

Storm name	Year	Storm intensity range ($m\,s^{-1}$)	Number of flights	Number of sondes
Bonnie	1998	50–52	5	61
Danielle	1998	33–37	6	92
Georges	1998	35–68	7	68
Bret	1999	52–57	1	16
Floyd	1999	47–63	4	33
Lili	2002	34–65	21	188
Fabian	2003	34–62	9	88
Isabel	2003	42–72	9	153
Frances	2004	45–64	13	138
Ivan	2004	35–72	27	203
Jeanne	2004	44–54	10	67
Dennis	2005	36–62	14	87
Katrina	2005	52–77	2	45
Rita	2005	34–77	17	161
Dean	2007	38–77	7	40
Gustav	2008	33–62	11	71
Paloma	2008	34–59	5	41
Bill	2009	44–59	16	124
Earl	2010	38–64	24	202
Totals			208	1878

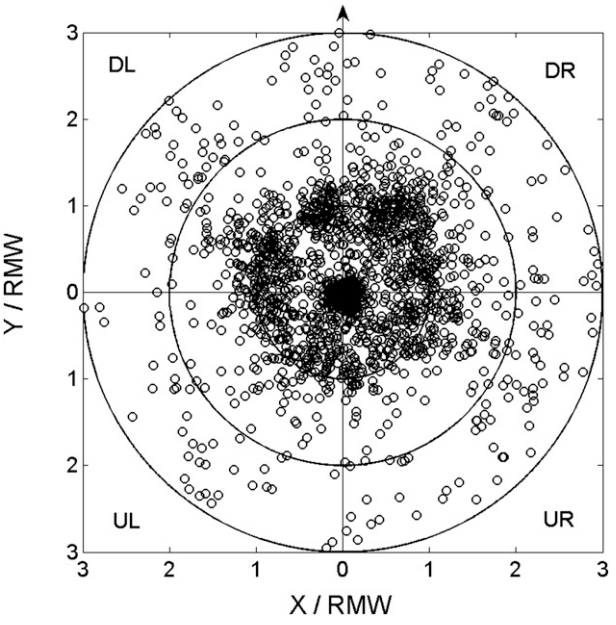

FIG. 1. Plot of the azimuthal distribution of the dropsonde data as a function of distance to the storm center normalized by the radius of maximum wind speed (RMW). Shear direction is to the top of the figure as indicated by the black arrow.

analyses, according to the National Hurricane Center's best-track dataset.

Figure 1 shows the data coverage relative to the storm center, with observation locations rotated with respect to the environmental vertical wind shear direction, showing a nearly even distribution in shear-relative azimuth. The storm characteristics, including the intensity V_{max}, radius of maximum wind (RMW), storm translational direction speed V_s, and environmental shear magnitude and direction (heading), are presented in Fig. 2. RMW is estimated using stepped-frequency microwave radiometer and flight-level wind data as detailed by Zhang and Uhlhorn (2012). The frequency distributions of V_{max}, RMW, and V_s indicate that observations represent a broad spectrum of storms (Fig. 2). Here, for each dropsonde, V_{max} and V_s and direction are obtained from the 6-hourly best-track database (Jarvinen et al. 1984) interpolated to the time of observation. Storm intensities are in the range $33 < V_{max} < 77\,m\,s^{-1}$, sizes in terms of RMW are $10 < R_{max} < 62$ km, and translational speeds are $0.8 < V_s < 12.3\,m\,s^{-1}$. The median storm intensity for the whole sample is $V_{max} = 112$ kt (1 kt = $0.5144\,m\,s^{-1}$) (Saffir–Simpson category 3), radius of maximum wind is $R_{max} = 31.8$ km, and storm translational speed is $V_s = 5.5\,m\,s^{-1}$. The 850–200-hPa environmental vertical wind shear is obtained from the Statistical Hurricane Intensity Prediction Scheme (SHIPS) database (DeMaria et al. 2005). The shear is derived from the National Centers for Environmental Predication (NCEP) operational global model analysis and defined as the vector difference of the mean winds within a 500-km radius from the storm center between 200 and 850 hPa (Kaplan et al. 2010). The shear magnitude ranges from 0 to 35 kt, with shear heading on average toward the northeast.

Dropsonde data are analyzed and grouped in a composite framework following the method used by Zhang et al. (2011). The composite analysis method has been widely used in previous studies investigating the hurricane inner core structure (e.g., Frank 1984; Lorsolo et al. 2010; Rogers et al. 2012), vertical wind profile structure (e.g., Franklin et al. 2003; Powell et al. 2003), and surface layer air–sea thermal structure (e.g., Cione et al. 2000; Zhang and Uhlhorn 2012). The advantage of the composite analysis method is that it provides a general characterization of the structure. The greatest drawback to compositing is that it tends to smooth possibly important structural details among a large number of storms.

The data are grouped as a function of the radius to the storm center r that is normalized by the radius of the maximum wind speed; that is, $r^* = r/\text{RMW}$. The center positions have been determined using the flight-level data to fix the storm center using the algorithm developed by Willoughby and Chelmow (1982). Data are composited through bin averaging with a radial bin width of $r^* = 0.2$ for the inner core ($r^* < 2$), and $r^* = 0.4$ for the outer part for four quadrants relative to the shear direction. Note that the outer core part of the analysis extends out

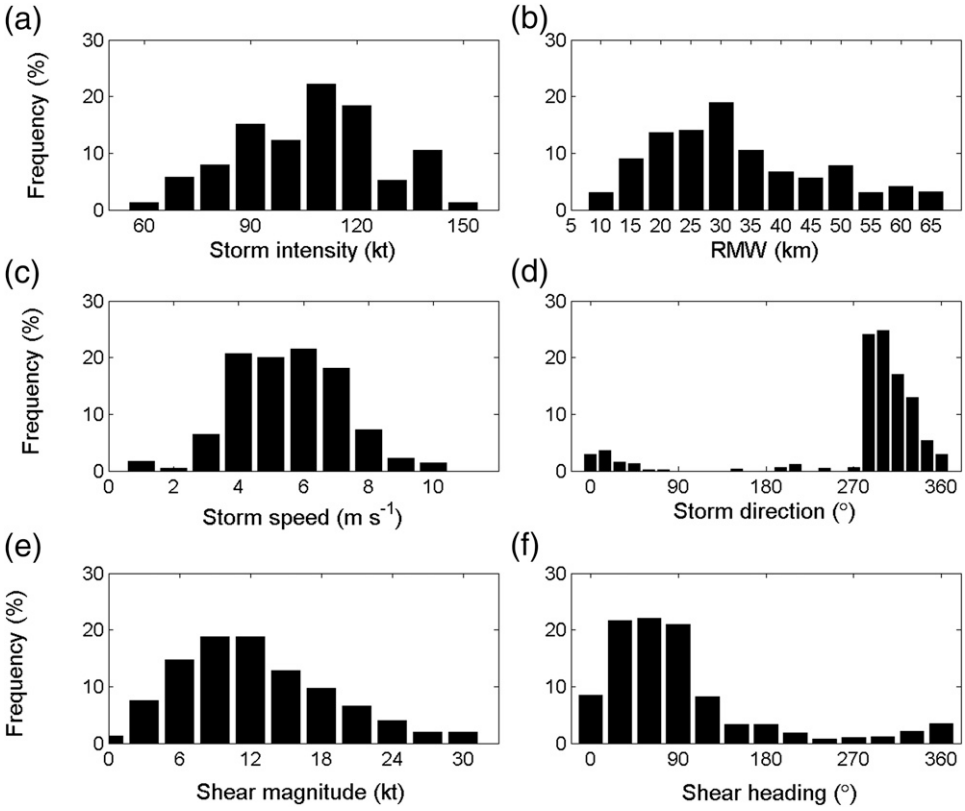

FIG. 2. Frequency distribution of dropsondes according to the corresponding (a) storm intensity, (b) RMW, (c) storm speed, (d) storm direction, (e) shear magnitude, and (f) shear heading rotated clockwise with 0° pointing to the north.

to $r^* = 3$ instead of $r^* = 5$ as in our previous study. This is due to sparse sonde coverage beyond $r^* = 3$, which limits asymmetric analysis accuracy. The data are also interpolated vertically every 10 m. For additional composite analysis methodology details, refer to Zhang et al. (2011) and Zhang and Uhlhorn (2012).

3. Results

First, quadrant-averaged boundary layer structure is analyzed relative to the shear direction. The four quadrants are defined counterclockwise as upshear left (UL), upshear right (UR), downshear right (DR), and downshear left (DL) quadrants. Winds are computed relative to storm motion by subtracting the storm-motion vector from the dropsonde-observed Cartesian wind vector before transforming to radial (Vr) and tangential (Vt) components relative to the storm center location. Figure 3 shows the r^*–z plots of the Vt for the four quadrants, showing the jetlike structure located at the eyewall ($r^* = 1$). The jet strength is largest in the DL quadrant. The height of the maximum Vt (h_{vtmax}) increases with increasing radius from the storm center for all shear-relative quadrants, reflecting the symmetric behavior of h_{vtmax} reported by Zhang et al. (2011). The difference in h_{vtmax} for the four quadrants in the eyewall is small, with h_{vtmax} located at approximately 500–700 m. The two quadrants left of the shear have higher h_{vtmax} than the right-side quadrants in the outer radii ($r^* > 1.5$). It is also found that h_{vtmax} is highest at the DL quadrant and lowest at the UR quadrant. Asymmetric structure for the total wind speed is similar to Vt, except that the height of the maximum wind speed is generally lower (not shown).

Radial wind composites are presented in Fig. 4, with the radial flow obtained from composites of Doppler radar data using different cases (Reasor et al. 2013) superimposed. Note that the radar composite is constructed using data from a smaller number of flights than in this study but with comparable values of the mean storm intensity, radius of maximum wind speed, and shear magnitude and direction (see Fig. 2 of Reasor et al. 2013). Figure 4 shows that the radial inflow and outflow structure in these two analyses generally agree with each other, in particular, for the azimuthal variation of boundary layer heights. The DR quadrant is found to have the deepest inflow layer, while the UR quadrant has

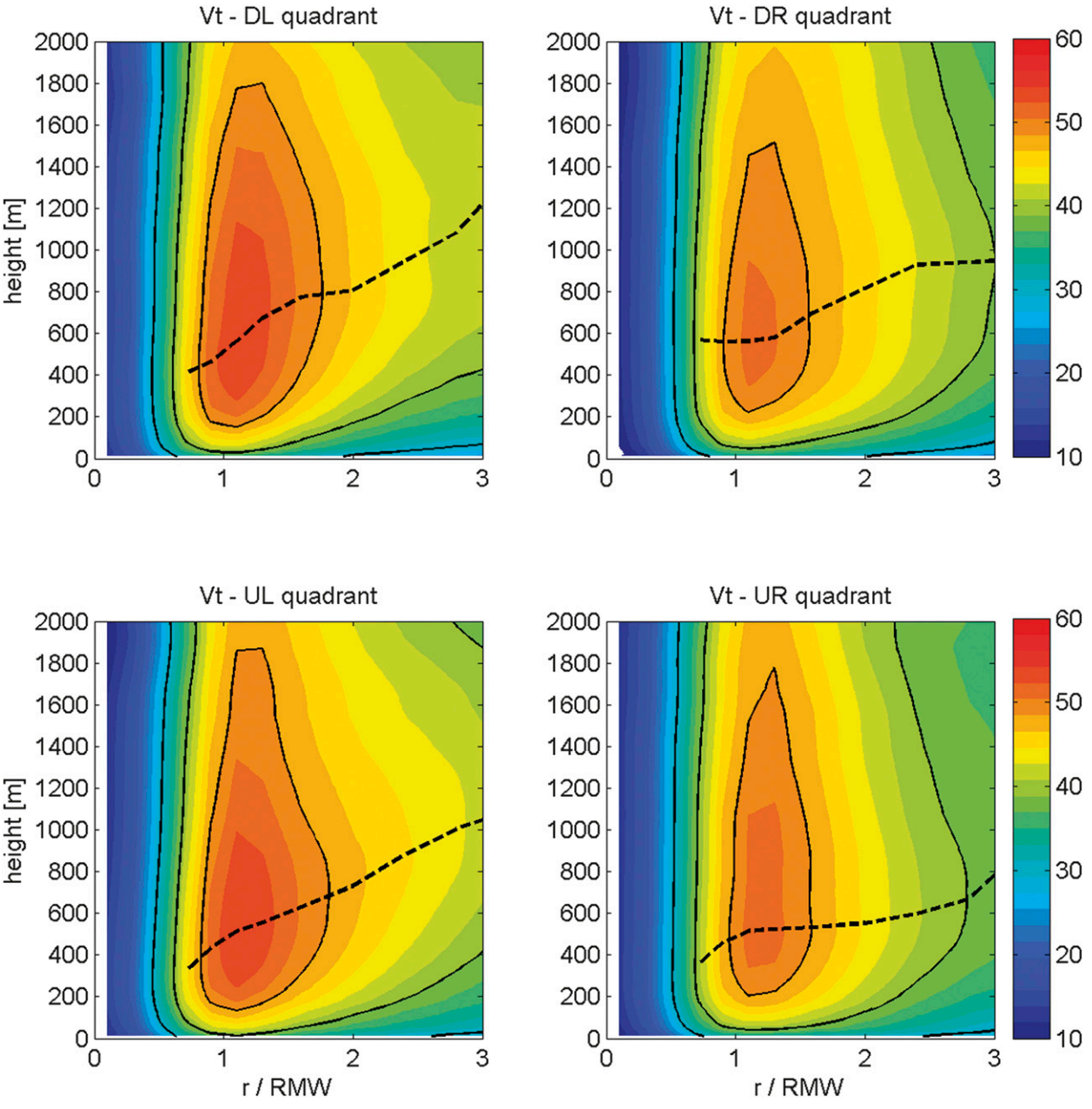

FIG. 3. Composite analysis result of the relative tangential wind velocity (with contour interval of 2 m s^{-1}) as a function of altitude and the normalized radius to the storm center for the four quadrants relative to the shear direction. The thick black lines in each panel are the 30, 40, and 50 m s^{-1} contours. The black dashed line in each panel depicts the height of the maximum tangential wind speed varying with radius.

the shallowest inflow layer from both the radar and dropsonde composites. The inflow layer in the UR quadrant from the dropsonde composite is generally shallower than 500 m, below the level that can be captured from the Doppler analyses (Reasor et al. 2013). On the other hand, both the radar and dropsonde data capture similar outflow structure above 500 m in the UR quadrant. The radial flow structure in the other quadrants is also generally consistent between dropsonde and Doppler composites. The difference in radial flow magnitude is partly due to different storms included in the analyses. Another reason for the difference is the resolution difference between the two sources of data. The vertical resolution of the dropsonde data (~10 m) is much higher than that of the radar data (~500 m), but the horizontal resolution of the radar data (~2 km) is

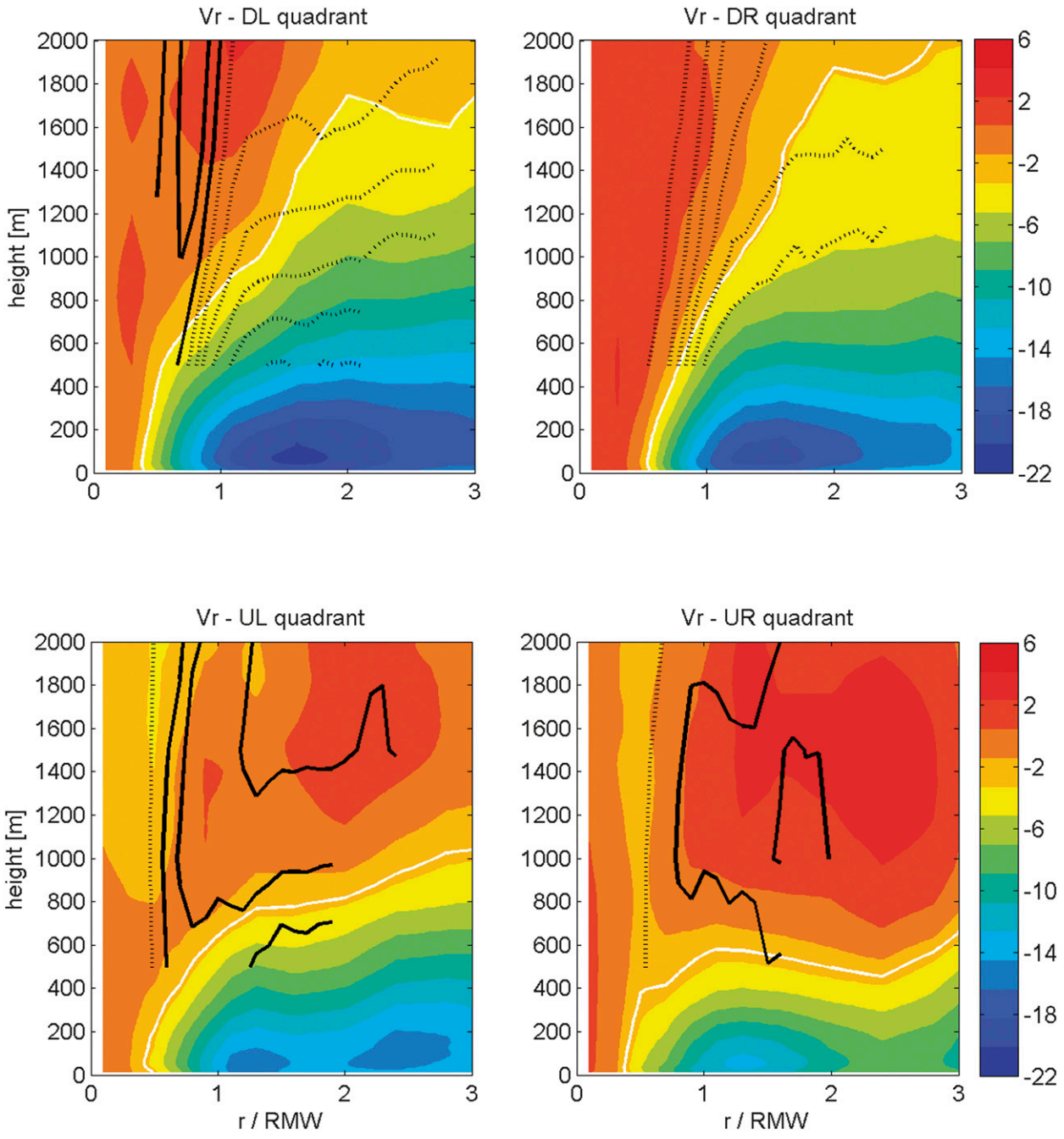

FIG. 4. Composite analysis result of the relative radial wind velocity (color shaded with contour interval of 2 m s^{-1}) as a function of altitude and the normalized radius to the storm center for the four quadrants relative to the shear direction. The white line in each panel represents the height of 10% peak inflow. Doppler radar composite results are shown in the black lines with solid lines representing outflow and dotted lines representing inflow with a contour interval of 0.5 m s^{-1}.

higher than that of the dropsonde composite (~5 km). Also, the radar data only extend down to 500 m (with limited coverage there), while the dropsonde data can extend all the way down to 10 m above the sea surface.

Furthermore, the dropsonde composite shows that the peak radial inflow is much larger in the downshear quadrants than that in the upshear quadrants. Figure 4 also shows that the DR quadrant has the strongest radial inflow at around 150 m above the surface. The DL quadrant has the strongest outflow above the inflow layer in the eyewall region, consistent with the radar composite.

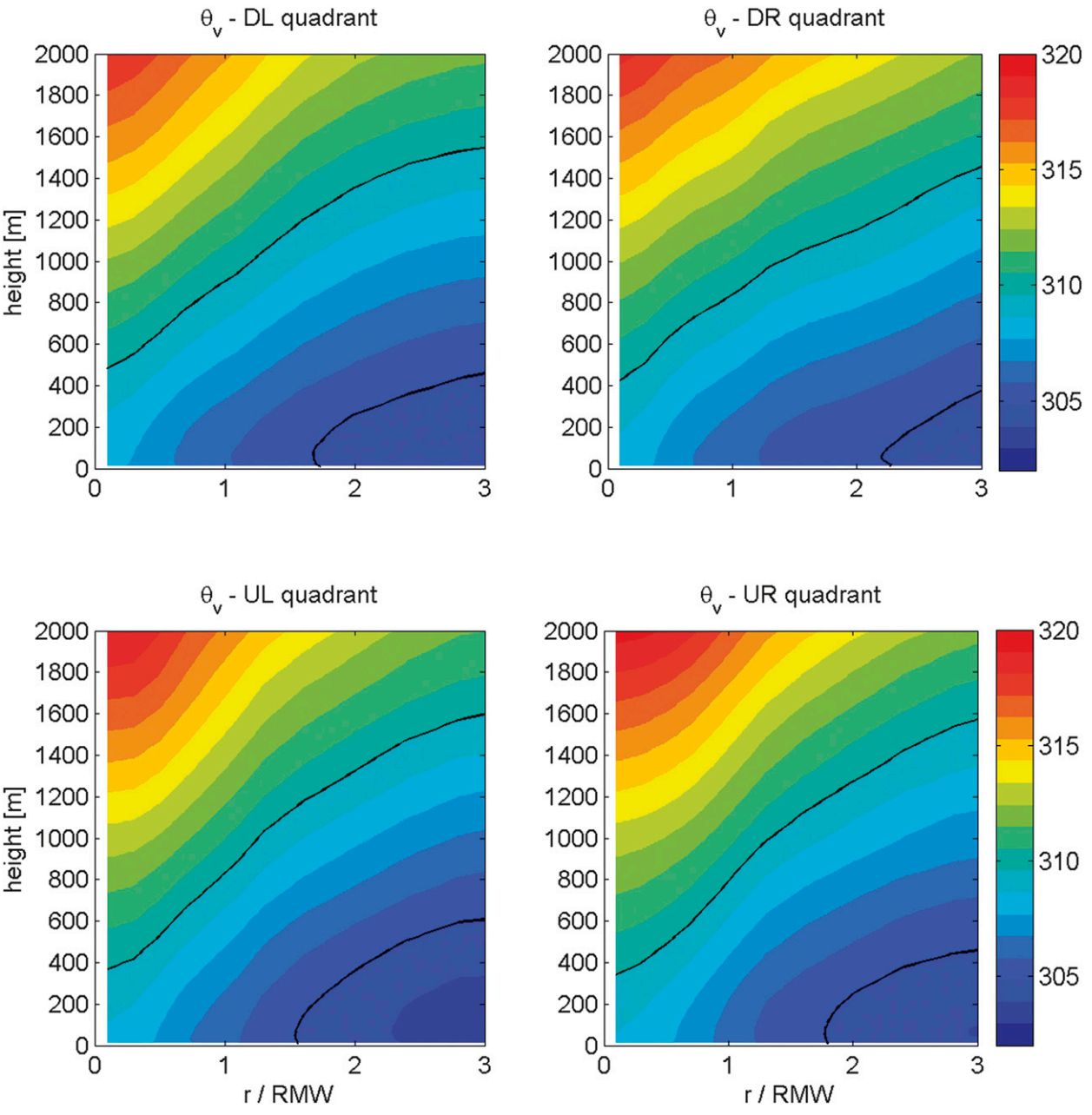

FIG. 5. Composite analysis result of the virtual potential temperature as a function of altitude and the normalized radius to the storm center for the four quadrants relative to the shear direction. The thick black lines are the 305- and 310-K contours. The contour interval is 1 K.

The r^*–z analysis of the virtual potential temperature (θ_v) is shown in Fig. 5. At first glance, the θ_v structure is similar for the four shear-relative quadrants. Following the method used by Zhang et al. (2011), the thermodynamic boundary layer height (i.e., the mixed layer depth) is defined as the height where θ_v increases by 0.5 K from the mean value of the data from the lowest 150 m. The field of (θ_v–$\theta_{v,150}$ is shown in Fig. 6, indicating that the mixed layer depth tends to increase with increasing distance from the storm center for all the shear-relative quadrants, consistent with previous axisymmetric analysis results. The mixed layer depth z_i is located at approximately 300 m in the eyewall, which is much shallower than the kinematic boundary layer heights (h_{vtmax} and h_{inflow}). The difference in z_i between the four quadrants is small, particularly in the eyewall region. In the outer core region ($r^* > 2.5$), the DL quadrant has the deepest mixed layer while the UR quadrant

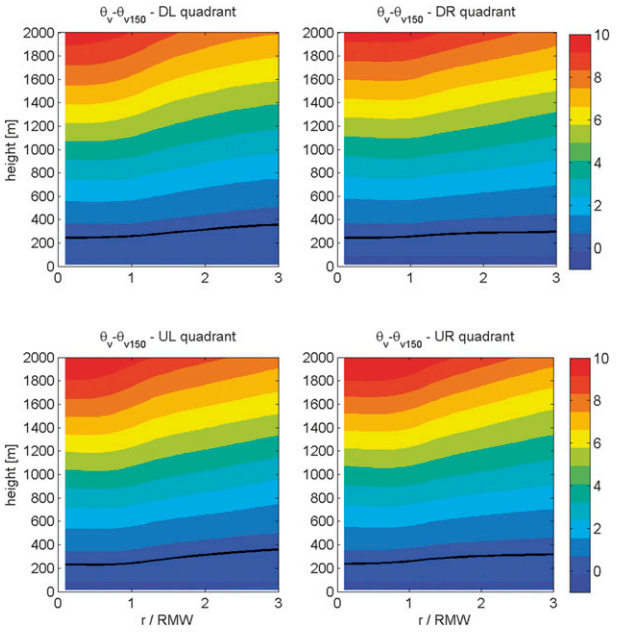

FIG. 6. As in Fig. 5, but for the difference of the virtual potential temperature at each level and its mean value in the lowest 150-m data. The thick black line denotes the 0.5 K difference contour.

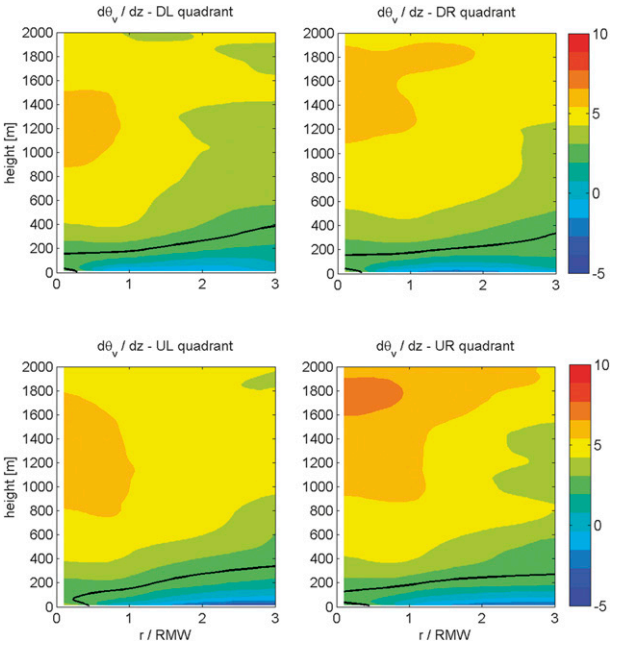

FIG. 7. As in Fig. 5, but the lapse rate of the virtual potential temperature. The thick black line denotes the $d\theta_v/dz = 3\,\mathrm{K\,km^{-1}}$ contour. The contour interval is $1\,\mathrm{K\,km^{-1}}$.

has the shallowest mixed layer in the outer core region, although the mixed layer depth difference is small (<100 m).

Zhang et al. (2011) tested another definition of the mixed layer depth using the height where the lapse rate of θ_v first exceeds $+3\,\mathrm{K\,km^{-1}}$. The mixed layer depth calculated using this definition (Fig. 7) is consistent with the former method (Fig. 6). Again, the mixed layer depths in the four quadrants are found to increase with increasing radius. This behavior agrees with that found by Zhang et al. (2011) in the azimuthally averaged boundary layer structure. Consistent with the behavior of mixed layer depth calculated using the former definition, the lapse-rate method shows a more pronounced radial dependence of the mixed layer depth in the left two quadrants than the right quadrants. In addition, there appears to be a slight increase in the static stability in the UR quadrant compared to other quadrants, suggesting a stronger eye inversion in this quadrant according to Fig. 7.

Our above analyses illustrate an interesting boundary layer asymmetric structure relative to the wind shear, which has not been well documented in previous studies. Both the dropsonde and radar composite analyses indicate a similar asymmetric pattern in the kinematic structure. We next focus on studying the thermodynamic structure asymmetry and its relationship to the asymmetry of convection as indicated by the radar reflectivity data.

Figure 8 shows the azimuthal variation of the quadrant-averaged temperature and specific humidity at two levels (1.5 km and 50 m) along with the radar reflectivity at 1.5 km in the eyewall region ($0.8 < r^* < 1.2$). An anticorrelation is found between the temperature and reflectivity fields for the four quadrants (Figs. 8a,c). The UR quadrant, which typically has the weakest radar reflectivity, is the warmest among the four quadrants. At upper levels (~1.5 km) the DL quadrant is the coolest when the radar reflectivity is the highest, which may be attributed to precipitation and associated evaporative cooling. This cooling is believed not to be related to instrument wetting error because almost all (~95%) previously observed cases for instrument wetting errors (Eastin et al. 2002a,b) were found in the presence of nonzero cloud water, but not in the boundary layer where air is generally unsaturated though close to saturation in heavy rain conditions (cf. Fig. 9a). The mean temperature near the sea surface (50 m) in the UL quadrant is even slightly cooler than that in the DL quadrant (Fig. 8c). It is speculated that this cooling in the UL quadrant is due to convective downdrafts observed in the radar composite (cf. Fig. 11b).

A positive correlation is found between the specific humidity and radar reflectivity at 1.5 km (Fig. 8b). This relationship is expected because of the precipitation helping to moisten the air (cf. Fig. 9a). The DL quadrant has the highest radar reflectivity, and the air in this

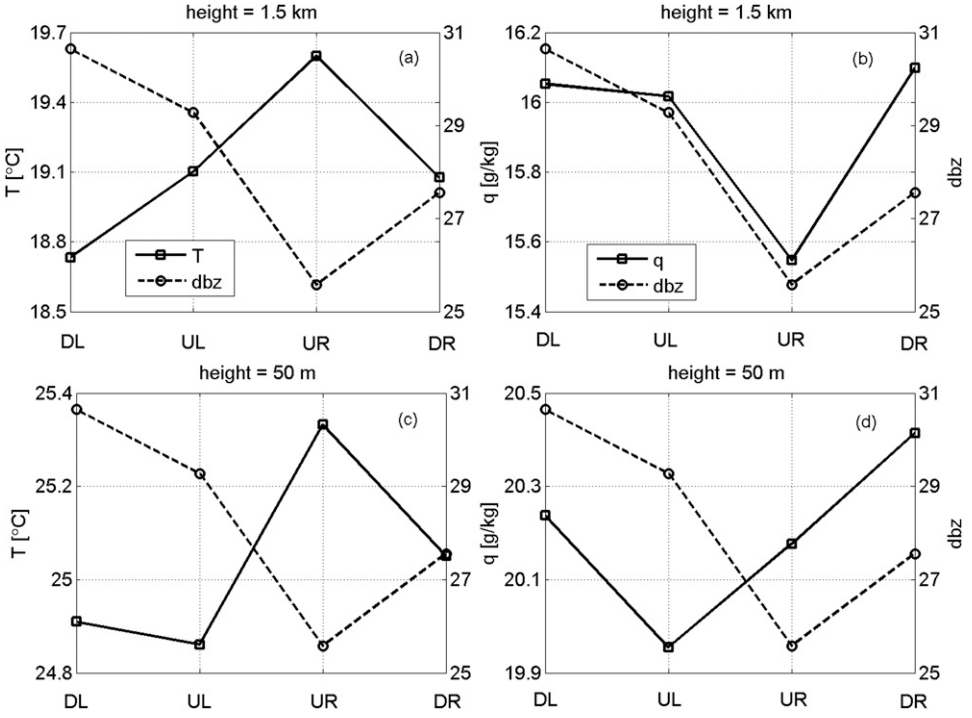

FIG. 8. Comparison between the dropsonde and radar composite analyses results in terms of shear-relative quadrant averages of (a) temperature at 1.5 km vs radar reflectivity at 1.5 km, (b) specific humidity 1.5 km vs radar reflectivity at 1.5 km, (c) temperature at 50 m vs radar reflectivity at 1.5 km wind velocity, and (d) specific humidity 50 m vs radar reflectivity at 1.5 km.

quadrant has the highest humidity. The variance in the relative humidity in the DL quadrant is the lowest (Fig. 9b) throughout the boundary layer, further confirming that the observed humidity and radar reflectivity structures are consistent for the two independent data sources.

Near the surface (~50 m), the correlation between the specific humidity and radar reflectivity is weaker compared to that above (Fig. 8d). The UL quadrant has the lowest specific humidity as compared to the UR quadrant where the relative humidity is the lowest (Fig. 9a) due to the large temperature difference (Fig. 8c). We note that the difference in mean specific humidity near the surface between the UL and DR quadrants (Fig. 8) is statistically significant at 95% confidence according to a Student's t test. There is also a statistically significant difference in the mean temperature in the UL and UR quadrants. The combined differences in temperature and specific humidity lead to significant difference in near-surface θ_e between the UL and DR quadrants; implications of this finding will be discussed below.

Vertical profiles of quadrant-averaged θ_e and 95% confidence intervals calculated from the analyzed data within that quadrant are shown in Figs. 10a and 10b, respectively, for the eyewall region ($0.8 < r^* < 1.2$). It appears that the UL quadrant has the lowest θ_e near the sea surface (<50 m). No statistically significant difference is found in θ_e between the UL and DL quadrants at all levels, but the mean θ_e difference between the DL and DR quadrants is statistically significant at 95% confidence level. Within the thermodynamic mixed layer (<250 m), θ_e increases from the UL quadrant to the UR quadrant to become a maximum in the DR quadrant. It is thought that an air parcel is cooled by strong rainfall and downdrafts as it exits the DL quadrant. Rotating through the UL and UR quadrants, the parcel acquires heat and moisture from surface fluxes, raising its θ_e. Convection occurs in an area of mesoscale lifting in the DR quadrant (cf. radar composites in Fig. 11b), where θ_e is the highest. Energy is then released by latent heating in the region of strong convection with heavy precipitation (DL quadrant). Convective downdrafts then bring down cool air to the surface with lower θ_e.

To further illustrate the above conceptual model, the near-surface (50 m) wavenumber-0 and wavenumber-1 (with all wavenumbers 2+ omitted) components of θ_e are shown in Fig. 11 along with radar reflectivity and vertical velocity composites (full fields) at 1.5 km. It appears that the peak θ_e and peak reflectivity are out of phase in the eyewall area. The peak reflectivity is located in the DL quadrant while the peak θ_e is located in the DR quadrant

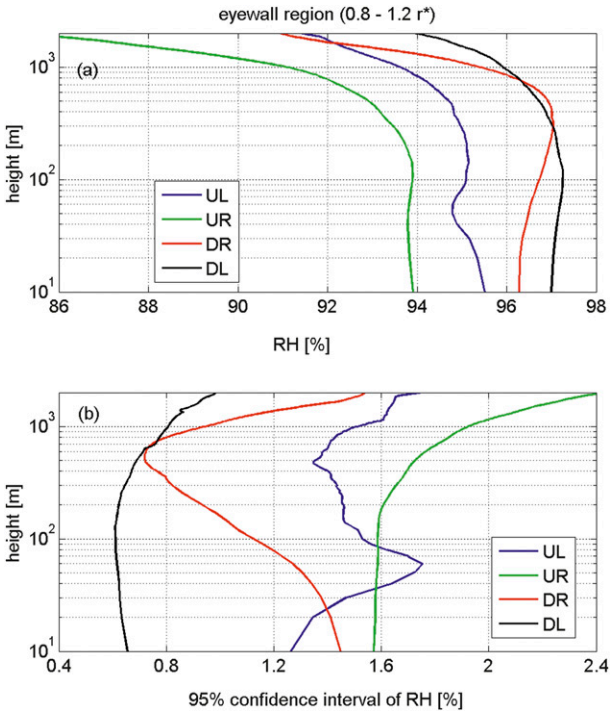

FIG. 9. Vertical profiles of (top) quadrant averages and (bottom) 95% confidence interval of relative humidity (RH) for the four quadrants relative to the shear direction. These averages are computed using data at the eyewall region ($r^* = 0.8$–1.2).

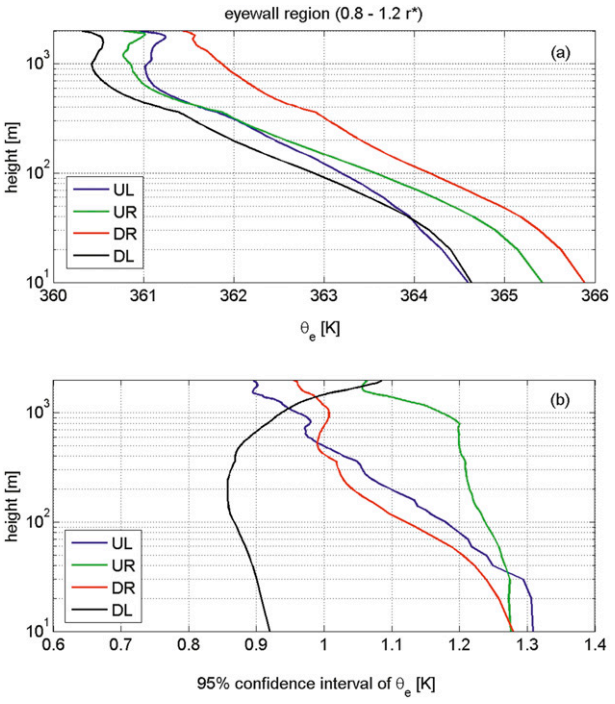

FIG. 10. As in Fig. 9, but for equivalent potential temperature (θ_e).

(Fig. 11a). On the other hand, the θ_e asymmetry tends to correlate with the asymmetry of vertical velocity, which is an indicator of updrafts or downdrafts. This θ_e asymmetry can be observed more clearly by removing the azimuthal-mean component at each radius (Fig. 12).

Figure 12 confirms that the peak reflectivity and θ_e are out of phase, while the asymmetry patterns of the vertical velocity and θ_e tend to correlate with each other. The large positive θ_e perturbation is virtually collocated with the peak updrafts in the downshear to DR quadrant, while the largest negative θ_e perturbation is found to be close to the strong downdrafts. This strongest θ_e asymmetry is observed inside the RMW (i.e., the annulus between $r^* = 0.7$–0.9). Following the method used by Molinari et al. (2013), we estimated the increase of θ_e from the surface moisture and heat fluxes using the observed values of surface wind, temperature, and humidity (see the appendix for details). The increase in θ_e ($\sim$+4 K) from the left of shear to the DR quadrant in the annulus with the peak wavenumber-1 asymmetry can be attributed to surface enthalpy fluxes. This suggests that our conceptual model for shear-induced asymmetry of convection in connection with boundary layer thermodynamics is logical within the context of boundary layer recovery.

4. Discussion and conclusions

The asymmetric low-level (i.e., hurricane boundary layer) structure in relation to the environmental vertical wind shear is investigated in the inner core region using a total of 1878 dropsondes from 19 hurricanes, and extends the symmetric analysis of Zhang et al. (2011). To the authors' knowledge, it is the first time that the asymmetric thermodynamic structure has been investigated in a shear-relative framework in the low-level inner core region using observational data. Here, we composite the data relative to the shear direction to investigate variations of the boundary layer height scales in the shear-relative framework. Beyond the boundary layer height scales, we also investigate the asymmetry of kinematic and thermodynamic fields at different levels in order to link the boundary layer structure and shear-induced asymmetry of convection. Comparisons in kinematic structure between the dropsonde and Doppler radar composites show consistent results, although there are some differences between these independent analyses that can be explained. It is believed that our results represent the general asymmetric structure of the hurricane boundary layer relative to the environmental wind shear. In addition, the radar reflectivity asymmetry is also consistent with the observed thermodynamic structure asymmetry from the dropsonde composites, in that the azimuthal

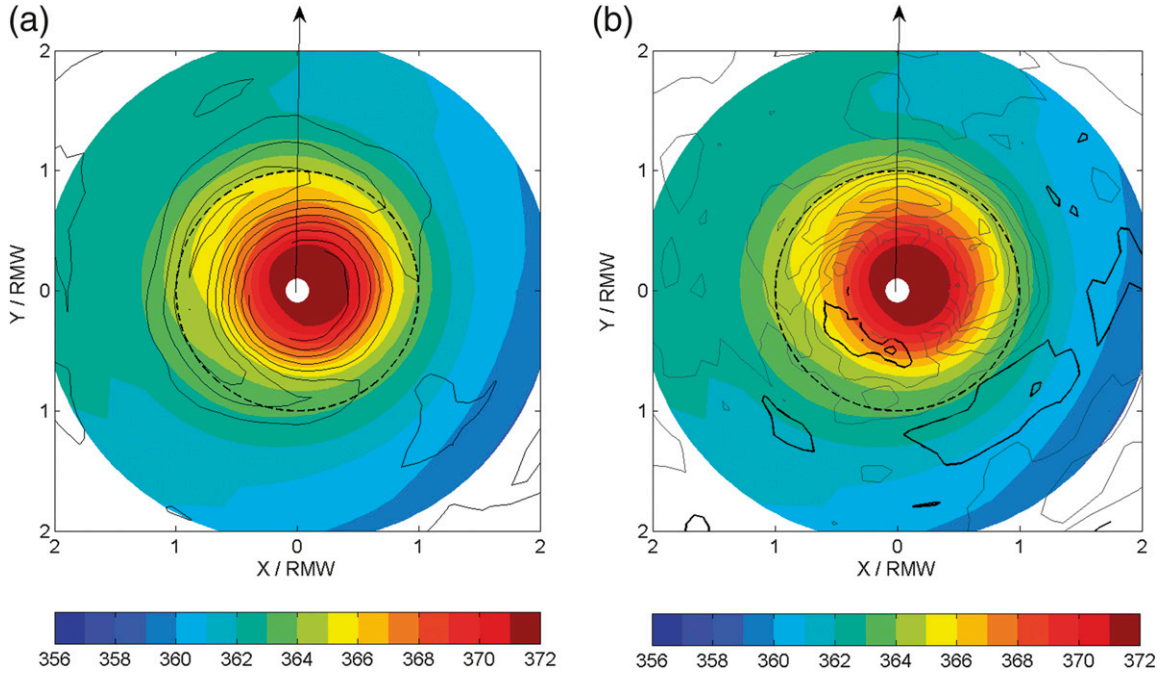

FIG. 11. (a) Plots of the wavenumber-0 and -1 components of equivalent potential temperature (color shaded in K) at 50 m with radar reflectivity at 1.5 km (contours in dBZ), (b) As in (a), but with contours of vertical velocity measured by radar at 1.5 km. The contour interval for radar reflectivity is 2 dBZ and that for vertical velocity is 0.2 m s^{-1}. In (b), gray contours represent updrafts and black contours represent downdrafts. Shear direction is shown by the black arrow. The thick dashed black line represents the radius of maximum wind speed.

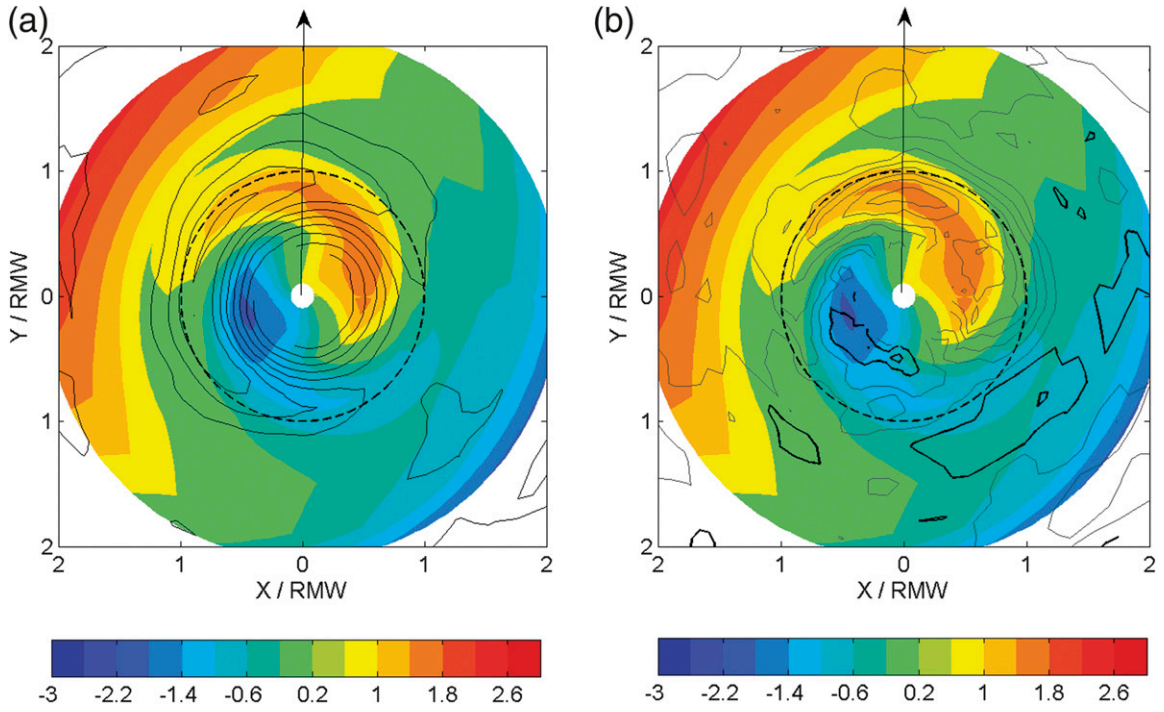

FIG. 12. As in Fig. 11, but for the wavenumber-1 component of equivalent potential temperature.

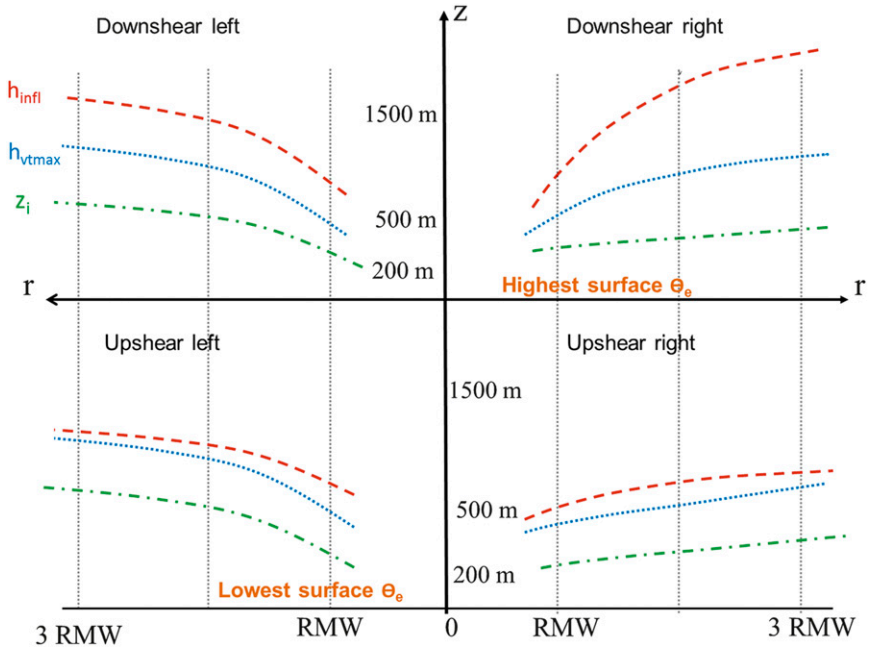

FIG. 13. Schematic diagram of the characteristic height scales of the hurricane boundary layer for the four quadrants relative to the shear direction. The height scales are based on the composite analysis of the dropsonde data; h_{infl} is the inflow layer depth (red dashed line); z_i is the mixed layer depth (green dash-dotted line); and h_{vmax} is the height of the maximum tangential wind speed (blue dotted line). Note that the notation for θ_e is limited to the eyewall region and within the surface layer.

variations of the temperature and humidity are correlated with that of the radar reflectivity.

Figure 13 is a schematic diagram summarizing the characteristic height scales such as the height of the maximum wind speed (h_{vtmax}), the inflow layer depth (h_{infl}), and the mixed layer depth (z_i) as a function of normalized distance ($r^* = r/\text{RMW}$) in the four shear-relative quadrants. Here each height scale is based on the dropsonde composite analysis result presented earlier. Our analyses show that there is still a clear separation between the thermodynamic and kinematic boundary layer heights when data are grouped in the shear-relative coordinates. Consistent with our previous findings based on the symmetric analysis, the kinematic boundary layer heights (i.e., h_{vtmax} and h_{inflow}) are found to increase with increasing radius from the storm center in all shear-relative quadrants. Again, the thermodynamic boundary layer height (z_i) is much shallower than the kinematic boundary layer height, which also tends to increase with increasing radius.

It is also found that heights of both the maximum wind speed and the tangential wind are within the inflow layer for all the quadrants. The storm-relative inflow layer is found to be deepest in the DR quadrant and shallowest in the UR quadrant. The difference in h_{vtmax} between the four shear-relative quadrants is relatively small in the eyewall region, as is the difference in the mixed layer depth. It is found that h_{vtmax} is higher in the two quadrants left of the shear than right of the shear. This left–right structural contrast is also found for the mixed layer depth. The variation of the mixed layer depth as a function of radius to the storm center is found to be smaller in the two quadrants right of shear than in those left of shear. Furthermore, all of the above mentioned height scales are found to be shallowest in the UR quadrant.

The decrease of the dynamical–kinematic boundary layer height with decreasing radius in the axisymmetric framework is consistent with the scaling height argument according to theories of rotating boundary layers (Eliassen 1971; Carrier 1971; Montgomery et al. 2001; Kepert 2001; Kepert and Wang 2001; Nolan 2005; Foster 2009; Zhang et al. 2009). Our data analyses show that the decrease of the kinematic boundary layer height with decreasing radius is also evident in the shear-relative framework. The asymmetric thermodynamic boundary layer height is also found to decrease with decreasing radius, although the slope is smaller than that for the kinematic boundary layer heights. This result supports the hypothesis by Zhang et al. (2011) that the mixed layer depth is also possibly controlled by boundary layer dynamics, in that the entire boundary layer depth is constrained by the increasing inertial stability toward the center.

The asymmetric thermodynamic and kinematic boundary layer heights are not correlated with the asymmetry of radar reflectivity. The mixed layer depths in the eyewall region for the four shear-relative quadrants are close to each other, suggesting that the mixed layer depth is not purely connected to the strength of convection. The most convectively active DL quadrant, as indicated by the radar reflectivity peak, does not have a deep mixed layer. Similarly, the UL quadrant, where the strongest downdrafts are observed, does not have a shallow mixed layer. It is likely that strong dynamic turbulent mixing in the eyewall makes the mixed layer depth similar for all the quadrants. This result implies that the mixed layer recovery argument in terms of mixed layer depth (e.g., Powell 1990) related to convective downdrafts associated with the outer core rainbands may not apply in the eyewall region containing the strongest winds. On the other hand, the mixed layer depth is found to be the shallowest in the UR quadrant at outer radii ($r^* > 2$) where downdrafts are observed in the radar composites. This behavior in mixed layer depth in the outer core is consistent with observations given by Barnes et al. (1983) and Powell (1990).

The asymmetric pattern of convection may be linked to the boundary layer thermodynamic asymmetry. Rotating through the UL and UR quadrants, parcels acquire heat and moisture from surface fluxes, raising their θ_e. When θ_e reaches a maximum value, convection is triggered in the DR quadrant in the presence of asymmetric mesoscale lifting as observed by the radar composites. Convective downdrafts transport cool and dry air to the surface and lower the value of θ_e in the DL and UL quadrants. Fueled by enthalpy fluxes as air parcels travel through the UR and DR quadrants, θ_e then increases again. This cycling process associated with wavenumber-1 surface θ_e asymmetry is believed to be directly tied to the shear-induced asymmetry of convection. We note that mesoscale lifting is also preferred on the downshear side as indicated from the radar composites (Reasor et al. 2013). It is not until parcels reach the DR quadrant where mesoscale lifting occurs that convection can occur.

Certainly, this is a complicated process including surface heat transfer, convective downdraft cooling, radial advection, and eye–eyewall mixing. Our analyses suggest a route for an air parcel to travel with its varying thermodynamic properties consistent with the shear-induced asymmetry of convection. Our thermodynamic conceptual model of how eyewall convection is triggered, matures, decays, and is reinitiated is in agreement with the explanation provided by Eastin et al. (2005) for the azimuthal distribution of buoyant convection (both up and down) in the eyewall. Their observational data at midlevels (altitude between 4 and 6 km) indicated that negatively buoyant downdraft cores (resulting from localized evaporative cooling and/or water loading) originate at upper levels left of the shear and accelerate downward while being advected cyclonically around to the upshear quadrants. These observational findings given by Eastin et al. (2005) at midlevels provided independent confirmation of the cycling process we propose here using data at low levels (altitudes below 3 km), and demonstrate the robustness of our results. This model is also supported by the boundary layer recovery analyses as detailed in the appendix. The analyses showed that the increase in near-surface θ_e from left of the shear to the DR quadrant within the annulus with strongest θ_e asymmetry can be entirely supported by surface heat and moisture fluxes, suggesting that this explanation is reasonable.

It should be noted that our analyses at this point cannot be used to test the paradigm of Riemer et al. (2010) on shear-induced weakening of TCs through the reduction of θ_e in the inflow layer. In their simulations, the shear direction is along the direction of motion. On average, our data show that the motion and shear direction differ by 60° to 120°. To fully test their paradigm, observations from a weakening storm moving in the same direction as the shear would be required. In addition, continuous measurements of both kinematic and thermodynamic fields over the life cycle of a weakening storm are necessary.

As the boundary layer dynamics in a rotating system are closely related to storm motion (Shapiro 1983; Kepert and Wang 2001), our future work will investigate the asymmetric boundary layer structure relative to the storm motion as well. Corbosiero and Molinari (2003) found that the asymmetry of lightning in tropical cyclones is related to storm motion, although the shear induced asymmetry dominates the motion effect. The asymmetry of reflectivity is found to be tied much more strongly to the shear than the storm motion effect as pointed out by Reasor et al. (2013). Our future work thus will test whether the shear-induced asymmetry of the boundary layer thermodynamics dominates the storm motion–induced asymmetry. Reasor et al. (2013) also found that the direction of vortex tilt is largely connected to the shear direction but with variations. Whether the boundary layer structural asymmetry is more correlated with wind shear or with vortex tilt can be tested using collocated dropsonde and Doppler radar data, which is beyond the scope of the current paper but will be an interesting research topic to be studied. Our future work will also include studying the difference in asymmetric boundary layer structure in storms with different shear magnitudes when more dropsonde data are processed.

Finally we note that the results presented in this study should be useful for evaluating numerical simulations for hurricane predictions. As part of NOAA's Hurricane Forecast Improvement Program (HFIP), this work provides a dataset for evaluating the representation of boundary layer structure in tropical cyclone model simulations.

Acknowledgments. This work was supported by the NOAA Hurricane Forecast Improvement Project (HFIP) with Award NA12NWS4680004. We gratefully acknowledge all the HRD scientists and crews from AOC who were involved in the Hurricane Research Division's field program collecting the data. We appreciate the efforts of all the scientists and researchers who helped collecting the dropsonde data during HRD's field campaigns. Without their efforts, this work would not have been possible. In particular, we are grateful to Kathryn Sellwood, Sim Aberson, and Neal Dorst for making all the raw dropsonde data available. We thank John Kaplan for providing the shear data from the SHIPS model. We also thank Joe Cione for helpful discussions. Jun Zhang is grateful to John Molinari for his constructive suggestions that improve the interpretation of the results. We also thank the reviewers for their comments that helped improve our paper.

APPENDIX

Changes in Near-Surface θ_e as a Result of Surface Fluxes

Following Molinari et al. (2013), we wish to estimate the time rate of change of θ_e at the levels near the surface (~50 m) as a result of sensible and latent heat fluxes from the ocean surface. Our purpose is to confirm that the observed changes in θ_e could be attributable to surface fluxes.

Surface sensible and latent heat fluxes are estimated using the bulk method with the exchange coefficients as follows:

$$F_H = \rho c_p C_h U_{10}(\mathrm{SST} - T_{10}), \tag{A1}$$

$$F_q = \rho L_v C_e U_{10}(q_0 - q_{10}), \tag{A2}$$

where U is surface wind speed, T is temperature, q is specific humidity, subscript 10 represents 10 m, ρ is air density, L_v is latent heat of vaporization, c_p is the specific heat of air (at constant pressure), C_h and C_e respectively represent the exchange coefficient for sensible heat and latent heat transfer, and SST is sea surface temperature. We use $c_p = 1004.64\,\mathrm{J\,kg^{-1}\,K^{-1}}$ and $L = 2.5 \times 10^6\,\mathrm{J\,kg^{-1}}$. Exchange coefficient values of $C_h = C_e = 1.2 \times 10^{-3}$ are based on recent observational studies (Zhang et al. 2008; Haus et al. 2010; Bell et al. 2012). All other variables in Eqs. (A1) and (A2) can be obtained from the dropsonde data except the SST. The mean value of T_{10}, q_{10}, and U_{10} averaged from the UL quadrant to DR quadrant in the eyewall are approximately 25°C, $20\,\mathrm{g\,kg^{-1}}$, and $40\,\mathrm{m\,s^{-1}}$, respectively. We conservatively assumed that the air–sea temperature contrast is 2.5°C, which gives SST ~ 27.5°C, following Cione et al. (2000). Using the values above gives surface sensible and latent heat fluxes of ~151 and $\sim 673\,\mathrm{W\,m^{-2}}$, respectively. These values are comparable to estimates in previous observational studies (e.g., Cione et al. 2000; Shay and Uhlhorn 2008; Bell et al. 2012).

Next, changes of θ and q at a certain level within the boundary layer produced by surface sensible and latent heat fluxes are given by

$$\frac{d\theta}{dt} = \frac{\theta}{c_p T}\left(-\frac{1}{\rho}\frac{\partial F_{\mathrm{Hz}}}{\partial z}\right) = \frac{\theta}{c_p T}\left(\frac{F_{\mathrm{H0}}}{\rho \Delta z}\right), \tag{A3}$$

$$\frac{dq}{dt} = \left(-\frac{1}{\rho L_v}\frac{\partial F_{\mathrm{qz}}}{\partial z}\right) = \frac{F_{\mathrm{q0}}}{\rho L_v \Delta z}. \tag{A4}$$

In Eqs. (A3) and (A4), it is assumed that the fluxes vary linearly with height from their value at the surface to the top of the boundary layer, which is ~700 m (i.e., the upper bound of the inflow layer depths of the four shear-relative quadrants) in this case. Note that the unit of T is in K instead of °C. Here F_{H0} and F_{q0} are given by Eqs. (A1) and (A2), respectively, and $\Delta z = 700$ m. At level of 50 m, the mean θ, T, and ρ are 297 K, 297.65 K, and $1.11\,\mathrm{kg\,m^{-3}}$. Substituting the values above to Eqs. (A3) and (A4) gives a θ change of $0.6\,\mathrm{K\,h^{-1}}$ and a q change of $1.1\,\mathrm{g\,kg^{-1}\,h^{-1}}$.

Finally, in order to determine boundary layer θ_e changes from the fluxes, we conduct logarithmic differentiation to the θ_e equation, which has the form

$$\theta_e = \theta \exp\left(\frac{L_v q}{c_p T_{\mathrm{LCL}}}\right), \tag{A5}$$

to obtain an equation for the rate of change of θ_e:

$$\frac{d\theta_e}{dt} = \frac{\theta_e}{\theta}\frac{d\theta}{dt} + \frac{\theta_e L_v}{c_p T_{\mathrm{LCL}}}\frac{dq}{dt}, \tag{A6}$$

where T_{LCL} represents the lifting condensation level temperature and is calculated following Bolton (1980). The computed mean values of θ_e, θ, and T_{LCL} are 365, 302, and 297 K respectively from the dropsonde composites. Variations in these quantities due to expected errors would not significantly change the result. Substituting

Eqs. (A1)–(A4) into Eq. (A6), it is found that θ_e increases at a rate of approximately 4.6 K h^{-1}.

For an air parcel to travel from the UL quadrant to the UR quadrant in the eyewall region ($r^* \sim 1$), it takes 56 min at an average RMW of ~32 km with mean wind speed at 50 m of ~45 m s^{-1}. During this period, θ_e increases by 4.3 K, which is much larger than the observed downshear increase in θ_e (~2 K), suggesting that surface enthalpy fluxes were sufficient to produce the observed boundary layer recovery in the eyewall region.

Recall that the strongest θ_e asymmetry is observed at the annulus inward from the RMW ($r^* \sim 0.8$) to the storm center. Here, it takes a relatively shorter time (~45 min) for a parcel to travel from the downdraft core (lowest θ_e) to the updraft core (θ_e) at this radius, resulting in less θ_e increase from surface fluxes. On the other hand, the boundary layer depth inward from the eyewall is much shallower (~21%) than that at the RMW, which would enhance flux convergence and thus warming and moistening. Using these values at this annulus along with other observed variables in Eqs. (A1)–(A6), a gain of ~4.4 K in θ_e from the surface enthalpy fluxes is estimated; which is again larger than the observed increase in θ_e (~4 K).

In the above calculations, we have neglected the effects of eye–eyewall mixing (Eastin et al. 2005) and dissipative heating (Bister and Emanuel 1998; Zhang 2010), which could enhance the gain in θ_e. We have also simplified the air parcel trajectory by assuming a circulating flow perpendicular to the radius. If an inflow angle of 20°–25° near the surface (Zhang and Uhlhorn 2012) were included the budget analysis, the gain in θ_e would be enhanced. But this gain in θ_e will be taken into account by the radial increase of θ_e toward the center apparent in Fig. 11. Indeed, our calculations are comparable to a more sophisticated calculation, such as Wroe and Barnes' (2003) θ_e budget along an inflow trajectory in Hurricane Bonnie (1998). Our argument in terms of modulation of the surface fluxes by convective downdrafts is also in common with that of Wroe and Barnes (2003). Overall, we believe our back-of-the-envelope estimates are reasonable, which suggests that the observed θ_e increase can be attributed to boundary layer recovery from surface fluxes.

REFERENCES

Barnes, G. M., 2008: Atypical thermodynamic profiles in hurricanes. *Mon. Wea. Rev.,* **136,** 631–643.

——, E. J. Zipser, D. Jorgensen, and F. Marks, 1983: Mesoscale and convective structure of a hurricane rainband. *J. Atmos. Sci.,* **40,** 2125–2137.

Bell, M. M., and M. T. Montgomery, 2008: Observed structure, evolution, and potential intensity of category 5 Hurricane Isabel (2003) from 12 to 14 September. *Mon. Wea. Rev.,* **136,** 2023–2046.

——, ——, and K. A. Emanuel, 2012: Air–sea enthalpy and momentum exchange at major hurricane wind speeds observed during CBLAST. *J. Atmos. Sci.,* **69,** 3197–3222.

Bender, M. A., 1997: The effect of relative flow on the asymmetric structure in the interior of hurricanes. *J. Atmos. Sci.,* **54,** 703–724.

Bister, M., and K. A. Emanuel, 1998: Dissipative heating and hurricane intensity. *Meteor. Atmos. Phys.,* **65,** 233–240.

Black, M. L., J. F. Gamache, F. D. Marks, C. E. Samsury, and H. E. Willoughby, 2002: Eastern Pacific Hurricanes Jimena of 1991 and Olivia of 1994: The effect of vertical shear on structure and intensity. *Mon. Wea. Rev.,* **130,** 2291–2312.

Bolton, D., 1980: The computation of equivalent potential temperature. *Mon. Wea. Rev.,* **108,** 1046–1053.

Braun, S. A., and L. Wu, 2007: A numerical study of Hurricane Erin (2001). Part II: Shear and the organization of eyewall vertical motion. *Mon. Wea. Rev.,* **135,** 1179–1194.

——, M. T. Montgomery, and Z. Pu, 2006: High-resolution simulation of Hurricane Bonnie (1998). Part I: The organization of eyewall vertical motion. *J. Atmos. Sci.,* **63,** 19–42.

Bryan, G. H., 2012: Effects of surface exchange coefficients and turbulence length scales on the intensity and structure of numerically simulated hurricanes. *Mon. Wea. Rev.,* **140,** 1125–1143.

——, and R. Rotunno, 2009: The maximum intensity of tropical cyclones in axisymmetric numerical model simulations. *Mon. Wea. Rev.,* **137,** 1770–1789.

Carrier, G. F., 1971: Swirling flow boundary layers. *J. Fluid Mech.,* **49,** 133–144.

Cione, J. J., P. G. Blasck, and S. H. Houston, 2000: Surface observations in the hurricane environment. *Mon. Wea. Rev.,* **128,** 1550–1561.

——, E. A. Kalina, J. A. Zhang, and E. W. Uhlhorn, 2013: Observations of air–sea interaction and intensity change in hurricanes. *Mon. Wea. Rev.,* **141,** 2368–2382.

Corbosiero, K. L., and J. Molinari, 2003: The relationship between storm motion, vertical wind shear, and convective asymmetries in tropical cyclones. *J. Atmos. Sci.,* **60,** 366–376.

Davis, C., and Coauthors, 2008: Prediction of landfalling hurricanes with the Advanced Hurricane WRF model. *Mon. Wea. Rev.,* **136,** 1990–2005.

DeMaria, M., 1996: The effect of vertical shear on tropical cyclone intensity change. *J. Atmos. Sci.,* **53,** 2076–2088.

——, M. Mainelli, L. K. Shay, J. A. Knaff, and J. Kaplan, 2005: Further improvements to the Statistical Hurricane Intensity Prediction Scheme (SHIPS). *Wea. Forecasting,* **20,** 531–543.

Eastin, M. D., P. G. Black, and W. M. Gray, 2002a: Flight-level thermodynamic instrument wetting errors in hurricanes. Part I: Observations. *Mon. Wea. Rev.,* **130,** 825–841.

——, ——, and ——, 2002b: Flight-level thermodynamic instrument wetting errors in hurricanes. Part II: Implications. *Mon. Wea. Rev.,* **130,** 842–851.

——, W. M. Gray, and P. G. Black, 2005: Buoyancy of convective vertical motions in the inner core of intense hurricanes. Part II: Case studies. *Mon. Wea. Rev.,* **133,** 209–227.

Eliassen, A., 1971: On the Ekman layer in a circular vortex. *J. Meteor. Soc. Japan,* **49,** 784–789.

Emanuel, K. A., 1986: An air–sea interaction theory for tropical cyclones. Part I: Steady-state maintenance. *J. Atmos. Sci.,* **43,** 585–605.

——, 1995: Sensitivity of tropical cyclones to surface exchange coefficients and a revised steady-state model incorporating eye dynamics. *J. Atmos. Sci.,* **52,** 3969–3976.

Foster, R. C., 2009: Boundary-layer similarity under an axisymmetric, gradient wind vortex. *Bound.-Layer Meteor.,* **131,** 321–344.

Frank, W. M., 1984: A composite analysis of the core of a mature hurricane. *Mon. Wea. Rev.,* **112,** 2401–2420.

——, and E. A. Ritchie, 2001: Effects of vertical wind shear on the intensity and structure of numerically simulated hurricanes. *Mon. Wea. Rev.,* **129,** 2249–2269.

Franklin, J. L., M. L. Black, and K. Valde, 2003: GPS dropwindsonde wind profiles in hurricanes and their operational implications. *Wea. Forecasting,* **18,** 32–44.

Haus, B., D. Jeong, M. A. Donelan, J. A. Zhang, and I. Savelyev, 2010: The relative rates of air–sea heat transfer and frictional drag in very high winds. *Geophys. Res. Lett.,* **37,** L07802, doi:10.1029/2009GL042206.

Heymsfield, G. M., J. B. Halverson, J. Simpson, L. Tian, and T. P. Bui, 2001: ER-2 Doppler radar investigations of the eyewall of Hurricane Bonnie during the Convection and Moisture Experiment-3. *J. Appl. Meteor.,* **40,** 1310–1330.

Hock, T. F., and J. L. Franklin, 1999: The NCAR GPS dropwindsonde. *Bull. Amer. Meteor. Soc.,* **80,** 407–420.

Jarvinen, B. R., C. J. Newmann, and M. A. S. Davis, 1984: A tropical cyclone data tape for the North Atlantic Basin, 1886–1983: Contents, limitations, and uses. NOAA Tech Memo. 22, 21 pp. [Available online at http://www.nhc.noaa.gov/pdf/NWS-NHC-1988-22.pdf.]

Jones, S. C., 1995: The evolution of vortices in vertical shear. I: Initially barotropic vortices. *Quart. J. Roy. Meteor. Soc.,* **121,** 821–851.

——, 2000: The evolution of vortices in vertical shear. III: Baroclinic vortices. *Quart. J. Roy. Meteor. Soc.,* **126,** 3161–3185.

Kaplan, J., and M. DeMaria, 2003: Large-scale characteristics of rapidly intensifying tropical cyclones in the North Atlantic basin. *Wea. Forecasting,* **18,** 1093–1108.

——, ——, and J. A. Knaff, 2010: A revised tropical cyclone rapid intensification index for the Atlantic and eastern North Pacific basins. *Wea. Forecasting,* **25,** 220–241.

Kepert, J. D., 2001: The dynamics of boundary layer jets within the tropical cyclone core. Part I: Linear theory. *J. Atmos. Sci.,* **58,** 2469–2484.

——, 2006a: Observed boundary layer wind structure and balance in the hurricane core. Part I: Hurricane Georges. *J. Atmos. Sci.,* **63,** 2169–2193.

——, 2006b: Observed boundary layer wind structure and balance in the hurricane core. Part II: Hurricane Mitch. *J. Atmos. Sci.,* **63,** 2194–2211.

——, and Y. Wang, 2001: The dynamics of boundary layer jets within the tropical cyclone core. Part II: Nonlinear enhancement. *J. Atmos. Sci.,* **58,** 2485–2501.

Lorsolo, S., J. A. Zhang, F. D. Marks, and J. Gamache, 2010: Estimation and mapping of hurricane turbulent energy using airborne Doppler measurements. *Mon. Wea. Rev.,* **138,** 3656–3670.

Molinari, J., and D. Vollaro, 2010: Distribution of helicity, CAPE, and shear in tropical cyclones. *J. Atmos. Sci.,* **67,** 274–284.

——, J. Frank, and D. Vollaro, 2013: Convective bursts, downdraft cooling, and boundary layer recovery in a sheared tropical storm. *Mon. Wea. Rev.,* **141,** 1048–1060.

Montgomery, M. T., H. D. Snell, and Z. Yang, 2001: Axisymmetric spindown dynamics of hurricane-like vortices. *J. Atmos. Sci.,* **58,** 421–435.

Nolan, D. S., 2005: Instabilities in hurricane-like boundary layers. *Dyn. Atmos. Oceans,* **40,** 209–236.

Ooyama, K. V., 1969: Numerical simulation of the life cycle of tropical cyclones. *J. Atmos. Sci.,* **26,** 3–40.

Powell, M. D., 1990: Boundary layer structure and dynamics in outer hurricane rainbands. Part II: Downdraft modification and mixed layer recovery. *Mon. Wea. Rev.,* **118,** 918–938.

——, P. J. Vickery, and T. A. Reinhold, 2003: Reduced drag coefficient for high wind speeds in tropical cyclones. *Nature,* **422,** 279–283.

Reasor, P. D., and M. T. Montgomery, 2001: Three-dimensional alignment and corotation of weak, TC-like vortices via linear vortex Rossby waves. *J. Atmos. Sci.,* **58,** 2306–2330.

——, and M. D. Eastin, 2012: Rapidly intensifying Hurricane Guillermo (1997). Part II: Resilience in shear. *Mon. Wea. Rev.,* **140,** 425–444.

——, M. T. Montgomery, F. D. Marks Jr., and J. F. Gamache, 2000: Low-wavenumber structure and evolution of the hurricane inner core observed by airborne dual-Doppler radar. *Mon. Wea. Rev.,* **128,** 1653–1680.

——, ——, and L. D. Grasso, 2004: A new look at the problem of tropical cyclones in vertical shear flow: Vortex resiliency. *J. Atmos. Sci.,* **61,** 3–22.

——, M. Eastin, and J. F. Gamache, 2009: Rapidly intensifying Hurricane Guillermo (1997). Part I: Low-wavenumber structure and evolution. *Mon. Wea. Rev.,* **137,** 603–631.

——, R. Rogers, and S. Lorsolo, 2013: Environmental flow impacts on tropical cyclone structure diagnosed from airborne Doppler radar composites. *Mon. Wea. Rev.,* **141,** 2949–2969.

Riemer, M., M. T. Montgomery, and M. E. Nicholls, 2010: A new paradigm for intensity modification of tropical cyclones: Thermodynamic impact of vertical wind shear on the inflow layer. *Atmos. Chem. Phys.,* **10,** 3163–3188.

Ritchie, E. A., and W. M. Frank, 2007: Interactions between simulated tropical cyclones and an environment with a variable Coriolis parameter. *Mon. Wea. Rev.,* **135,** 1889–1905.

Rogers, R., S. Chen, J. Tenerelli, and H. Willoughby, 2003: A numerical study of the impact of vertical shear on the distribution of rainfall in Hurricane Bonnie (1998). *Mon. Wea. Rev.,* **131,** 1577–1599.

——, S. Lorsolo, P. Reasor, J. Gamache, and F. Marks, 2012: Multiscale analysis of tropical cyclone kinematic structure from airborne Doppler radar composites. *Mon. Wea. Rev.,* **140,** 77–99.

Rotunno, R., Y. Chen, W. Wang, C. Davis, J. Dudhia, and G. J. Holland, 2009: Large-eddy simulation of an idealized tropical cyclone. *Bull. Amer. Meteor. Soc.,* **90,** 1783–1788.

Schubert, W. H., M. T. Mongomery, R. K. Taft, T. A. Guinn, S. R. Fulton, J. P. Kossin, and J. P. Edwards, 1999: Polygonal eyewalls, asymmetric eye contraction, and potential vorticity mixing in hurricanes. *J. Atmos. Sci.,* **56,** 1197–1223.

Shapiro, L. J., 1983: The asymmetric boundary layer flow under a translating hurricane. *J. Atmos. Sci.,* **40,** 1984–1998.

Shay, L. K., and E. W. Uhlhorn, 2008: Loop Current response to Hurricanes Isidore and Lili. *Mon. Wea. Rev.,* **136,** 3248–3274.

Shelton, K. L., and J. Molinari, 2009: Life of a six-hour hurricane. *Mon. Wea. Rev.,* **137,** 51–67.

Simpson, R. H., and H. Riehl, 1958: Mid-tropospheric ventilation as a constraint on hurricane development and maintenance. Preprints, *Tech. Conf. on Hurricanes,* Miami, FL, Amer. Meteor. Soc., D4.1–D4.10.

Sitkowski, M., and G. M. Barnes, 2009: Low-level thermodynamic, kinematic, and reflectivity fields of Hurricane Guillermo (1997) during rapid intensification. *Mon. Wea. Rev.,* **137,** 645–663.

Smith, R. K., and M. T. Montgomery, 2010: Hurricane boundary-layer theory. *Quart. J. Roy. Meteor. Soc.,* **136,** 1665–1670.

——, ——, and N. Van Sang, 2009: Tropical cyclone spin-up revisited. *Quart. J. Roy. Meteor. Soc.,* **135,** 1321–1335.

Tang, B., and K. Emanuel, 2010: Midlevel ventilation's constraint on tropical cyclone intensity. *J. Atmos. Sci.,* **67,** 1817–1830.

——, and ——, 2012: Sensitivity of tropical cyclone intensity to ventilation in an axisymmetric model. *J. Atmos. Sci.,* **69,** 2394–2413.

Wang, Y., and G. J. Holland, 1996: Tropical cyclone motion and evolution in vertical shear. *J. Atmos. Sci.,* **53,** 3313–3332.

Willoughby, H. E., and M. Chelmow, 1982: Objective determination of hurricane tracks from aircraft observations. *Mon. Wea. Rev.,* **110,** 1298–1305.

Wroe, D. R., and G. M. Barnes, 2003: Inflow layer energetics of Hurricane Bonnie (1998) near landfall. *Mon. Wea. Rev.,* **131,** 1600–1612.

Zhang, J. A., 2010: Estimation of dissipative heating using low-level in situ aircraft observations in the hurricane boundary layer. *J. Atmos. Sci.,* **67,** 1853–1862.

——, and E. W. Uhlhorn, 2012: Hurricane sea surface inflow angle and an observation-based parametric model. *Mon. Wea. Rev.,* **140,** 3587–3605.

——, P. G. Black, J. R. French, and W. M. Drennan, 2008: First direct measurements of enthalpy flux in the hurricane boundary layer: The CBLAST results. *Geophys. Res. Lett.,* **35,** L14813, doi:10.1029/2008GL034374.

——, W. M. Drennan, P. G. Black, and J. R. French, 2009: Turbulence structure of the hurricane boundary layer between the outer rainbands. *J. Atmos. Sci.,* **66,** 2455–2467.

——, R. F. Rogers, D. S. Nolan, and F. D. Marks, 2011: On the characteristic height scales of the hurricane boundary layer. *Mon. Wea. Rev.,* **139,** 2523–2535.